

Halide diffusion in mixed-halide perovskites and heterojunctions

Viren Tyagi,[†] Mike Pols,[†] Geert Brocks,^{†,‡} and Shuxia Tao^{*,†}

[†]Department of Applied Physics and Science Education, Eindhoven University of Technology, 5600 MB, Eindhoven, The Netherlands

[‡]Computational Chemical Physics, Faculty of Science and Technology and MESA+ Institute for Nanotechnology, University of Twente, 7500 AE, Enschede, The Netherlands

E-mail: s.x.tao@tue.nl

Abstract

Migration of halide defects guides ion transport in metal halide perovskites and controls the kinetics of halide mixing and phase separation. We study the diffusion of halide vacancies and interstitials in $\text{CsPb}(\text{I}_x\text{Br}_{1-x})_3$ and $\text{CsPbI}_3/\text{CsPbBr}_3$ heterojunctions by molecular dynamics simulations using neural network potentials trained on density functional theory calculations. We observe enhanced diffusion of both vacancies and interstitials in the mixed halide compounds compared to the single halide ones, as well as a difference in mobility between Br and I ions in the mixed compound. Diffusion across heterojunctions is governed by the interface structure, where a Br-rich interface blocks migration of vacancies in particular, but an I-rich interface is permeable.

Introduction

Metal halide perovskites have gained traction in optoelectronic applications such as photovoltaics and light-emitting diodes.^{1–3} One of their strong points is chemical flexibility, where the perovskite ABX_3 structure allows for mixing different organic or inorganic cations (A), metal cations (B), and halide anions (X). Through compositional alloying, the physical properties such as band gaps and band offsets can be tuned, and at the same time this stabilizes the perovskite structure.^{4–6} For instance, mixing Br into CsPbI_3 lowers the temperature at which it transitions to the α (black) phase, and is less prone to degrade into the photo-inactive δ (yellow) phase,⁷ thereby improving the phase stability of this material. The currently most stable metal halide perovskites ABX_3 comprise a mix of X halide anions, as well as organic/inorganic A cations.^{8,9}

Although these alloys are stable under dark conditions, continuous light exposure commonly leads to demixing of I and Br ions^{10–12} and consequently the formation of low band gap I-rich domains and high band gap Br-rich domains.¹³ In previous work we presented a thermodynamic theory for light-induced halide segregation, based on the free energy gain

of photocarriers assembled in domains with a halide composition that has a lower band gap than the starting mixed phase.^{14,15} The growth of such domains is then stimulated by this thermodynamic driving force. While the origin of halide phase segregation is thermodynamic, the kinetics of this process are poorly understood, and a fundamental strategy for blocking or slowing down the kinetics is missing.

Microscopically, the most likely candidate for mass transport in these materials is the migration of halide defects.¹⁶ Halide perovskites are relatively soft materials and have a substantial concentration of defects.^{17–19} Halide point defects are generally considered the dominant mobile species.²⁰ The relative importance of vacancies versus interstitials seems to depend somewhat on the particular operational conditions and techniques used in different experimental studies, and may also reflect the different conditions under which the materials are synthesized.^{21–25}

From a modeling perspective, the most straightforward calculations make use of density functional theory (DFT) calculations on static structures along predicted migration paths to obtain diffusion barriers.^{21,26–28} Such migration paths may however be difficult to find. In addition, they may also not be sufficiently representative, as such modeling relies on one or a small number of transition states being adequate for describing diffusion. Irrespective of that point, halide perovskites display different phases as a function of temperature, so DFT calculations on $T = 0$ K structures may not describe diffusion at room or higher temperatures very well.

Molecular dynamics (MD) is a technique to simulate mass transport at the atomistic level directly, which also takes into account finite-temperature effects. Until recently, MD simulations have yielded limited information on diffusion in halide perovskites, as empirical model force fields tend to be too crude, and ab initio MD simulations are computationally too expensive to reach the required time and length scales for ion migration. Machine learned force fields (MLFFs) have advanced the capabilities of MD simulations, by combining a near ab initio accuracy with a computational cost only an order of magnitude above empirical

models.^{29–31} Moreover, by carefully selecting the ab initio reference data for training, MLFFs can describe the dynamics of a material at various electronic states.³²

In recent work we utilized atomic descriptor-based machine learned force fields^{33–36} to study the migration of different charged states of iodide interstitials and vacancies in CsPbI_3 .³⁷ We found that negative iodide interstitials and positive iodide vacancies, the most stable charge states for their respective defect type, migrate at similar rates at room temperature. In contrast, oppositely charged defects, i.e. positive iodide interstitials and negative iodide vacancies, migrate at much slower rates.

In the current work, we focus on the ion migration in mixed $\text{CsPb}(\text{I}_x\text{Br}_{1-x})_3$ compounds, where diffusion of point defects may involve both I and Br interstitials, as well as vacancies, and can depend on the local I versus Br environment.²⁷ We perform ns-long molecular dynamics (MD) simulations using MLFFs to quantify the migration behavior of halide defects in mixed $\text{CsPb}(\text{I}_x\text{Br}_{1-x})_3$. In particular, we focus on halide diffusion through interfaces between CsPbI_3 and CsPbBr_3 layers and study the initial phases of halide mixing. To conclude, we examine the stability of a CsPbI_3 nanodomain embedded in a CsPbBr_3 matrix and vice versa with respect to halide mixing at the interfaces induced by defect migration.²⁷

Methods

MLFFs based on Gaussian approximation potentials (GAPs)^{34,35} with smooth overlap of atomic position (SOAP) descriptors^{33,36} can accurately capture the diffusion of point defects, as we demonstrated in previous work on CsPbI_3 .³⁷ Likewise, they are suited to describe defect migration in CsPbBr_3 , as shown in SI note 1. However, they suffer from a poor scaling with the number of different chemical species, such as occurs in mixed $\text{CsPb}(\text{I}_x\text{Br}_{1-x})_3$ compounds.

Although, message passing neural network (MPNN) potentials^{38,39} overcome this shortcoming, global message passing gives them a poor computational scaling with system size. The Allegro neural network architecture⁴⁰ keeps the message passing local and is $E(3)$ -

equivariant (e3nn),⁴¹ which restrains the scaling with size and complexity of the system, see the SI note 2. As a result of this, an efficient MLFF for long-time scale MD simulations on large systems. Here, we train an Allegro model, as implemented in the NequiP package,³⁹ to generate a neural network potential (NNP) for halide interstitial and vacancy defects in $\text{CsPb}(\text{I}_{0.5}\text{Br}_{0.5})_3$.

The datasets for training and validating the network are generated using the on-the-fly module as implemented in VASP,^{34,42} where structures are sampled from 100 ps long MD runs. Energies, forces, and stress tensors are obtained from density functional theory (DFT) calculations with the PBE+D3-BJ exchange-correlation functional,^{43,44} for a set of structures selected through Bayesian inference, to ensure sufficient variance in the local environments. The training and validation sets are generated using $2 \times 2 \times 2$ cubic supercells of randomly mixed $\text{CsPb}(\text{I}_{0.5}\text{Br}_{0.5})_3$ with one halide point defect for a negatively charged halide interstitial (I_X^-), or a positively charged halide vacancy (V_X^+). Details of the training procedure are explained in the SI note 3.

The accuracy of the NNP energies can be explored, for instance, by comparing migration barriers along paths generated using the climbing image nudged elastic band (CI-NEB) technique⁴⁵ with those calculated by DFT along the same paths. The computed energies for vacancies and interstitials in randomly mixed $\text{CsPb}(\text{I}_{0.5}\text{Br}_{0.5})_3$ systems are given in Figure 1a-d. The difference between the migration barriers calculated using DFT and the NNP is less than 0.08 eV in all cases, indicating the NNP accurately probes the energy landscape for defect migration. The details of the CI-NEB calculations and calculated migration barriers are given in the SI note 4.

The NNP model is used to perform ns-long MD simulations in LAMMPS⁴⁶ on $6 \times 6 \times 6$ cubic supercells of bulk $\text{CsPb}(\text{I}_x\text{Br}_{1-x})_3$ with one halide point defect, interstitial or vacancy. To test the accuracy of the forces generated by the NNP, we sample structures from MD simulations at 600 K, and calculate the forces by DFT. Comparing these to the NNP forces for the system for which the NNP was developed, i.e., randomly mixed $\text{CsPb}(\text{I}_{0.5}\text{Br}_{0.5})_3$, gives

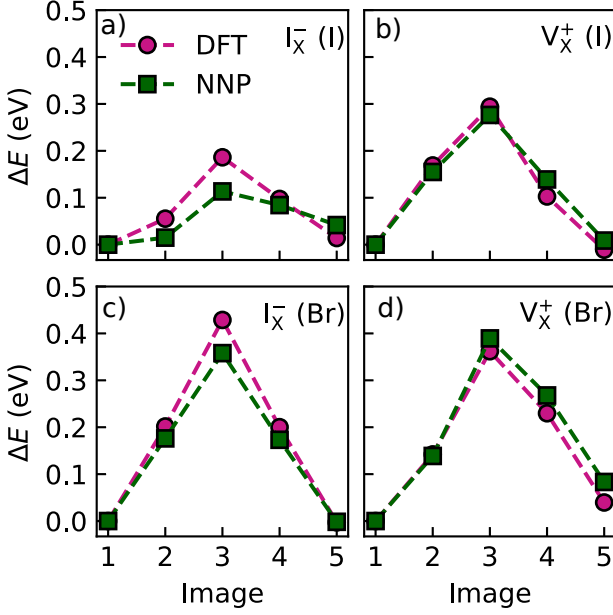


Figure 1: Energies along CI-NEB migration paths for I-mediated interstitial (a) and vacancy (b), and for Br-mediated interstitial (c) and vacancy (d) in $\text{CsPb}(\text{I}_{0.5}\text{Br}_{0.5})_3$ from DFT and NNP calculations. Zero is set at the energy minima.

$R^2 = 0.95$ and a mean absolute error (MAE) $\leq 51 \text{ meV}/\text{\AA}$ for forces acting on all atoms, and $R^2 \geq 0.94$ and MAE $\leq 56 \text{ meV}/\text{\AA}$ for forces acting on atoms in the defect environment, see the SI note 4. Using the same NNP in MD simulations on the pure compounds, CsPbI_3 or CsPbBr_3 , gives a very similar accuracy in the forces, see SI figure S11, which is a strong indication of the transferability of the NNP among $\text{CsPb}(\text{I}_x\text{Br}_{1-x})_3$ compounds for $0 \leq x \leq 1$.

Besides studying the diffusion of halide defects in $\text{CsPb}(\text{I}_x\text{Br}_{1-x})_3$, the NNP force field is also used to investigate migration of halide defects across interfaces between mono-halide layers, as well as halide mixing starting from mono-halide cubic nanodomains. The supercell size, temperature range, number of runs, and simulation time per run for all these systems are given in Table 1. The volume is kept constant during these runs, where the lattice constants for different halide concentrations in $\text{CsPb}(\text{I}_x\text{Br}_{1-x})_3$ are extracted from MD runs at constant temperature and pressure, see the SI note 5.

Table 1: The cubic supercell size, temperature range, simulation time per MD run, and number of runs used for the different systems in this study.

Model	Supercell	Temperature (K)	time (ns)	number of runs
Mixed halide	$6 \times 6 \times 6$	500 – 600	2	5
Interfaces	$16 \times 6 \times 6$	600	2	5
Nanodomains	$8 \times 8 \times 8$	600	10	1

Results

Diffusion in $\text{CsPb}(\text{I}_{0.5}\text{Br}_{0.5})_3$

Migration behavior is studied in randomly mixed $\text{CsPb}(\text{I}_{0.5}\text{Br}_{0.5})_3$ with one halide point defect, vacancy or interstitial, added. We choose vacancy V_X^+ or interstitial I^-_X , $X = \text{I}$ or Br , in their most stable charge states, as they occur under intrinsic or moderately doped conditions.¹⁸ To ensure sufficient migration events for statistics, MD runs are performed at elevated temperatures in the range 500-600 K. The details of these production runs are given in the SI note 6. To compare with the pure systems, we also perform MD simulations for the pure systems CsPbI_3 and CsPbBr_3 . For the data obtained for CsPbI_3 , see Ref.³⁷ The training and production run details for CsPbBr_3 and the diffusion behavior of other charge states of halide point defects are reported in SI note 1.

In characterizing halide defect diffusion in these systems it makes no sense to trace a specific type of halide ion, as migration typically proceeds via kick-out processes. Therefore, we use both halide species to extract the diffusion coefficient using the Einstein relation, which links the slope of the mean square displacement to time

$$D = \frac{1}{6} \lim_{t \rightarrow \infty} \frac{d}{dt} \left\langle \sum_{i=1}^N \|\mathbf{r}_i(t + t_0) - \mathbf{r}_i(t_0)\|^2 \right\rangle_{t_0}; \quad t > t_0, \quad (1)$$

where N is the number of atoms of a particular atomic species in the simulation box, and \mathbf{r}_i are the atomic positions.

In the following we will label diffusion coefficients by interstitial or vacancy, according

to the starting situation of each MD run. In the temperature and time ranges studied one observes multiple sequential kick-out events, so the actual species that is migrating can change over the trajectory. However, when starting with a single vacancy (interstitial), then one vacancy (interstitial) remains present; no additional long-lived defects are created.

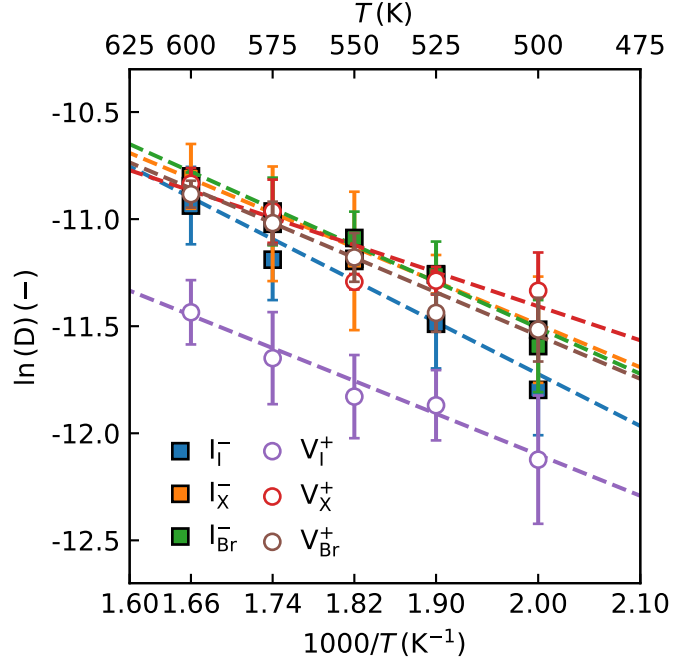


Figure 2: Temperature-dependent diffusion coefficients of halide interstitials (I^-) and vacancies (V^+) in pure $CsPbI_3$ (I), randomly mixed $CsPb(I_{0.5}Br_{0.5})_3$ (X), and pure $CsPbBr_3$ (Br). The filled square and open circle symbols represent halide interstitials and vacancies, respectively. The dashed lines represent fits to an Arrhenius expression, and the error bars represent the standard error in mean at each point.

Diffusion coefficients are given in Figure 2. They are extracted by applying Eq. 1 to the runs for the mixed-halide compound and similar systems created for the single-halide compounds. Comparing $CsPbI_3$ and $CsPbBr_3$ one observes that diffusion coefficients of Br and I interstitial, I_{Br}^- and I_I^- , in the temperature range 500-600 K are very similar, i.e., within 30% or so, with that of the I interstitial higher. The difference between the diffusion coefficients of Br and I vacancies, V_{Br}^+ and V_I^+ , is slightly larger, approximately a factor of two, with that of the I vacancy being the larger of the two. In the mixed $CsPb(I_{0.5}Br_{0.5})_3$ system the two halide species can change positions dynamically. As a first analysis we look at

the migration of the halide species X without distinguishing between Br and I. The diffusion coefficients for X interstitials and vacancies are remarkably close to those found in the pure systems, but slightly closer to the values found in CsPbBr_3 , in particular for the vacancy.

The diffusion coefficients can be fitted with an Arrhenius expression

$$D = D_0 \exp \left(-\frac{E_a}{k_B T} \right). \quad (2)$$

The fits are given in Figure 2, and the extracted activation energies (E_a) and pre-exponential factors (D_0) are given in Table 2. The error bars reflect the quality of the linear regression fit.

The activation energies are generally quite low and also quite close to one another. However, the barriers for interstitial diffusion are somewhat higher than those for vacancy diffusion. Likewise, the diffusion barriers in the mixed $\text{CsPb}(\text{I}_{0.5}\text{Br}_{0.5})_3$ halide are somewhat lower than in the pure compounds. Extrapolating the Arrhenius expression to room temperature, $T = 300$ K, one obtains values for the diffusion coefficients in the range 10^{-7} - 10^{-6} cm^2s^{-1} , see Table 2. The extrapolated diffusion coefficients of vacancies and interstitials in the mixed halide are approximately a factor of two larger than those in the pure compounds. In a similar fashion, the diffusion coefficients of vacancies are approximately a factor of two larger than those of interstitials.

Table 2: Activation energies (E_a) and pre-exponential factors (D_0) extracted from the Arrhenius fits, and extrapolated diffusion constants (D_{300K}) at room temperature for halide interstitial (I^-) and vacancy (V^+) defects in pure CsPbI_3 (I), randomly mixed $\text{CsPb}(\text{I}_{0.5}\text{Br}_{0.5})_3$ (X), and pure CsPbBr_3 (Br).

System	E_a (eV)	D_0 ($\times 10^{-3} \text{ cm}^2\text{s}^{-1}$)	D_{300K} ($\times 10^{-7} \text{ cm}^2\text{s}^{-1}$)
I_I^-	0.21 ± 0.03	1.08 ± 0.77	3.2
I_X^-	0.17 ± 0.04	0.54 ± 0.46	7.5
I_Br^-	0.19 ± 0.03	0.75 ± 0.43	4.8
V_I^+	0.16 ± 0.03	0.24 ± 0.19	4.9
V_X^+	0.13 ± 0.02	0.25 ± 0.12	16.4
V_Br^+	0.17 ± 0.02	0.53 ± 0.22	7.4

In principle, Eq. 1 also allows for decomposing the migration behavior of halide intersti-

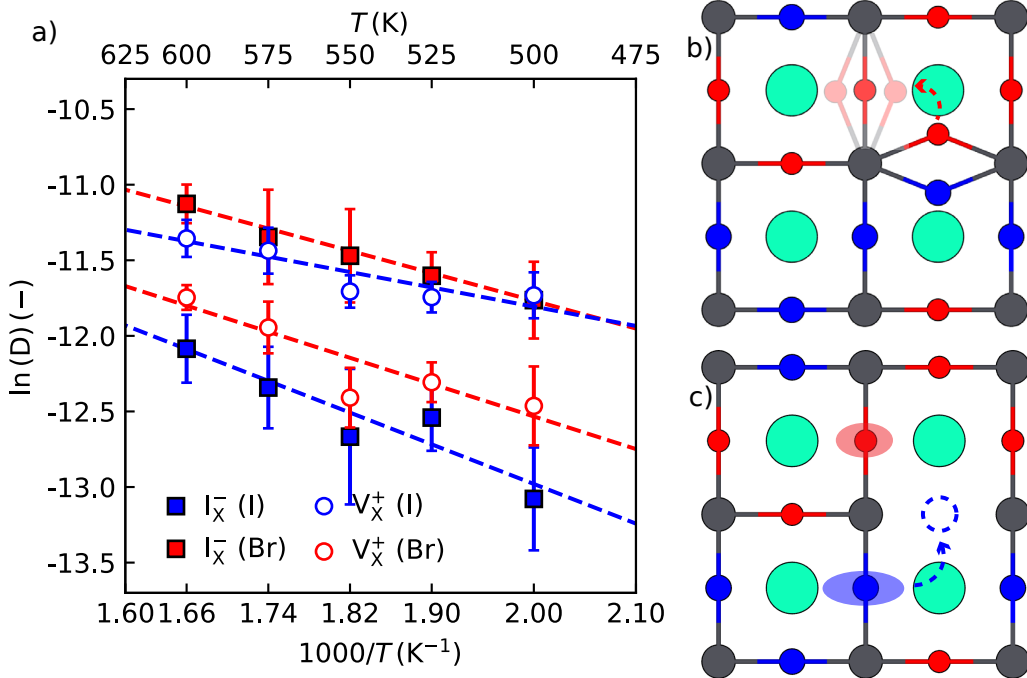


Figure 3: a) Halide species decomposed temperature-dependent diffusion coefficients of halide interstitials and vacancies in $\text{CsPb}(\text{I}_{0.5}\text{Br}_{0.5})_3$. Blue is for I, and red is for Br. The filled square symbols represent halide interstitials, and the open circle symbols represent halide vacancies. The dashed lines represent the fits to an Arrhenius expression, and the error bars represent the standard error in mean at each point. Schematic representation of the diffusion paths for (b) halide interstitial and (c) halide vacancy defects in $\text{CsPb}(\text{I}_{0.5}\text{Br}_{0.5})_3$. The arrows represent the migration directions of the ions.

tials and vacancies in the $\text{CsPb}(\text{I}_x\text{Br}_{1-x})_3$ down to halide species, i.e., distinguishing between Br and I. Diffusion coefficients for each species are given in Figure 3a). As it turns out, diffusion does not depend on the species, Br or I, initially chosen to represent interstitial or vacancy. As diffusion proceeds via kick-out processes, after a few of those events, the dominant species takes over. Regarding interstitials the Br species migrates faster than the I species, irrespective of the starting species of interstitial. Remarkably, for vacancies it is the other way around, i.e., I vacancies migrate faster than Br vacancies.

Interstitials and vacancies have opposite charge, so in an electric field they move in opposite directions. As the negatively charged interstitials will be driven to the anode, it will lead to a surplus of Br there. At the same time, the positively charged vacancies migrate to the cathode, which promotes a net flux of I in the direction of the anode. In an electric

field the two processes, interstitial- and vacancy-mediated diffusion, thus tend to compensate one another as a driving force for halide separation.

Arrhenius fits, Eq. 2, are shown in Figure 3a, with the parameters and the extrapolation to room temperature given in Table 3. These results confirm the trends discussed in the previous paragraph. Halide interstitials migrate an order of magnitude faster through Br than through I. Meanwhile, halide vacancies migrate faster through I than through Br. Focusing on the dominant migration mechanisms, migration of Br interstitials and I vacancies is roughly equally fast.

Table 3: Activation energies (E_a) and pre-exponential factors (D_0) extracted from the Arrhenius fits to diffusion coefficients decomposed according to halide species in $\text{CsPb}(\text{I}_{0.5}\text{Br}_{0.5})_3$ and diffusion constants (D_{300K}) extrapolated to room temperature.

System	E_a (eV)	D_0 ($\times 10^{-3} \text{ cm}^2\text{s}^{-1}$)	D_{300K} ($\times 10^{-7} \text{ cm}^2\text{s}^{-1}$)
I_X^- (I)	0.22 ± 0.06	0.43 ± 0.51	0.87
I_X^- (Br)	0.15 ± 0.04	0.29 ± 0.26	8.8
V_X^+ (I)	0.11 ± 0.02	0.08 ± 0.05	11.4
V_X^+ (Br)	0.18 ± 0.04	0.24 ± 0.19	2.3

To rationalize halide diffusion in mixed $\text{CsPb}(\text{I}_{0.5}\text{Br}_{0.5})_3$, we examine the defect geometries along the migration paths. The most stable configuration of a halide interstitial I_X^- is the bridge structure shown schematically in Figure 3b).^{17,47} In $\text{CsPb}(\text{I}_{0.5}\text{Br}_{0.5})_3$, a Pb–BrBr–Pb bridge configuration is more frequently observed than a Pb–IBr–Pb bridge configuration, both of which are observed significantly more than Pb–II–Pb bridge configuration, see the SI note 7. We conclude that the more prevalent a configuration is, the more stable it is. On the basis of occupation numbers, SI Figure S16, and assuming that these are determined by Boltzmann factors, we estimate an energy difference between the Pb–IBr–Pb bridge and the Pb–BrBr–Pb bridge of 34.5 meV, and between the Pb–II–Pb bridge and the Pb–BrBr–Pb bridge of 143.9 meV at 600 K. As I is much less likely to be found in an interstitial position than Br, the latter is the main species that causes diffusion of interstitial defects, as also shown in Figure 3.

By contrast, the halide vacancy has a preference for diffusion by I. The Pb–Br bond

is stronger than a Pb–I bond, suggesting that the latter can be more easily broken to let an I fill the vacancy, Figure 3c). Consistent with that notion, the I ions fluctuate more around their mean position, indicating a flatter energy landscape, than Br ions (SI note 8). Therefore, I ions would jump more easily to fill a vacancy, and hence form the dominant species for diffusion via vacancies.

A result regularly observed in simple materials is that compressive strain hinders interstitial diffusion, and tensile strain promotes it, whereas, in contrast, compressive strain promotes vacancy diffusion, and tensile strain hinders it.^{48,49} The general reasoning is that compression stabilizes the vacancy and destabilizes the interstitial, decreasing the diffusion barriers of the former and increasing those of the latter, whereas tension has the opposite effects. There are many exceptions to be found, but diffusion in $\text{CsPb}(\text{I}_{0.5}\text{Br}_{0.5})_3$ follows this rule. The lattice parameter of $\text{CsPb}(\text{I}_{0.5}\text{Br}_{0.5})_3$ is in between that of the pure compounds CsPbBr_3 and CsPbI_3 . From the perspective of Br, $\text{CsPb}(\text{I}_{0.5}\text{Br}_{0.5})_3$ is under tensile strain, whereas from the perspective of I it is under compressive strain. Hence, both the diffusion of Br interstitials and that of I vacancies in $\text{CsPb}(\text{I}_{0.5}\text{Br}_{0.5})_3$ should be promoted, which indeed it does considering Tables 2 and 3.

Our results are in qualitative agreement with those obtained in experiments by McGovern *et al.* on mixed $\text{MAPb}(\text{I}_x\text{Br}_{1-x})_3$ perovskites.⁵⁰ Compared to the pure I or Br perovskites, halide migration in mixed-halide perovskites has a lower activation energy and a larger diffusion coefficient, cf. Table 2. In addition, in the mixed-halide perovskite one finds two sets of diffusion coefficients and activation energies, describing the migration of the Br and I ions respectively, cf. Table 3. Full quantitative agreement with experiments on $\text{MAPb}(\text{I}_x\text{Br}_{1-x})_3$ cannot be expected, as the A cation (MA methylammonium versus Cs) is likely to have some influence on the ion migration behavior.

Diffusion across interfaces

Besides $\text{CsPb}(\text{I}_x\text{Br}_{1-x})_3$ where the Br and I are randomly mixed on an atomic scale, it is interesting to look at halide migration in materials comprising larger domains of pure CsPbI_3 and CsPbBr_3 . This occurs, for instance, when a material in a phase-separated state is kept in a dark environment.¹⁴ The simplest model geometry of such a state consists of layers of the pure compounds, as illustrated in Figure 4a, with planar interfaces along the $\langle 100 \rangle$ direction. At the interfaces between the pure I- and Br-perovskites, Pb atoms are coordinated partially by I and partially by Br atoms.

We consider the two extreme cases, an I-rich interface where the Pb atoms are coordinated by five I atoms and one Br atom, and a Br-rich interface with Pb atoms coordinated by five Br atoms and one I atom (Figure 4a). The calculated difference between the static formation energies of these interfaces is very small, 2.5 meV per Pb atom at the interface, see the SI note 9. As this is much smaller than $k_B T$ at room temperature, we conclude that both these interfaces are equally likely to form under equilibrium conditions.

Our model system consists of alternating layers of CsPbBr_3 and CsPbI_3 , each layer eight CsPbX_3 sublayers deep, where the interfaces are either all I-rich or all Br-rich, Figure 4a. We use an in-plane 6×6 supercell, and start with a defect, vacancy or interstitial, positioned at a specific interface. The supercell dimensions are obtained by the procedure described in the SI note 9. As we have two different interfaces and two different defects, this gives us four different cases in total. For each case we run a 2 ns MD simulation at $T = 600$ K, and repeat this five times for each system, while monitoring the position of the defect. As a result, Figure 4b-e shows the defect occupancies of the individual lead halide sublayers accumulated over all MD runs.

Starting with the vacancy, it clearly has a preference for residing in the CsPbBr_3 layer, Figure 4b and c. One could map occupancies N onto an energy landscape E_{X_j} , $\text{X} = \text{Br}, \text{I}$ and j the CsPbX_3 sublayer index from a Boltzmann expression $N \propto \exp[-E_{\text{X}_j}/k_B T]$, $T = 600$ K, between the two sublayers near the center of the CsPbBr_3 and CsPbI_3 layers one then

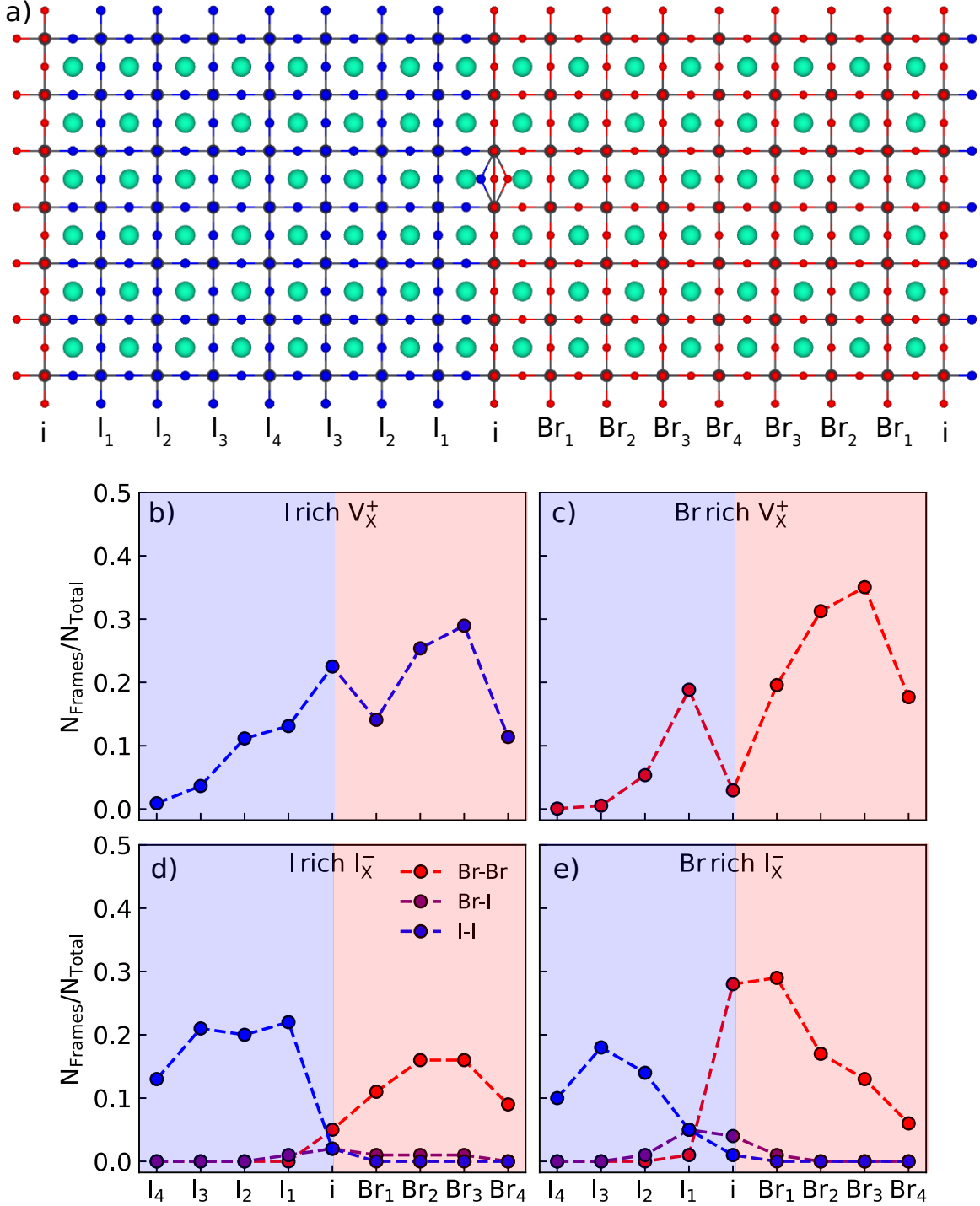


Figure 4: (a) Bulk interface and layers away from the interface in $16 \times 6 \times 6$ cubic supercell of $\text{CsPb}(\text{I}_x\text{Br}_{1-x})_3$, with 2 Br-rich interfaces along the periodic boundaries. Defect occupancy at different layers ($N_{\text{Frames}}/N_{\text{Total}}$) of (b) halide vacancy for I-rich interfaces, (c) halide vacancies for Br-rich interfaces, (d) halide interstitials for I-rich interfaces, and (e) halide interstitials for Br-rich interfaces.

finds an energy difference $E_{\text{I}_3} - E_{\text{Br}_3} > 100$ meV.

Comparing I-rich and Br-rich interfaces, there is a remarkable difference between of finding a vacancy there. Whereas the I-rich interface easily incorporates a vacancy, leading to an occupancy comparable to that of the CsPbBr_3 layer, the Br-rich interface actually repels vacancies. Again, mapping onto an energy gives an interface barrier $E_i \approx 130$ meV. The consequence is that I-rich interfaces are very permeable for the diffusion of vacancies, whereas Br-rich interfaces hinder the diffusion.

The interstitial gives a more complex picture. As interstitials diffuse by means of kick-out processes, they can change character, i.e., a Br interstitial can become an I interstitial in the next diffusion step and vice versa. The effects of these kick-out processes are visible in Figure 4d and e, where the occupancies of $\text{Pb}-\text{II}-\text{Pb}$ and $\text{Pb}-\text{BrBr}-\text{Pb}$ bridges are high in the CsPbI_3 and CsPbBr_3 layers, respectively, but there is no crossover of these bridges into the other layer.

For the Br-rich interface, mixed $\text{Pb}-\text{IBr}-\text{Pb}$ bridges are found at or very near the interface, with negligible occupancy further from the interface. Interestingly, also in this case the I-rich interface behaves differently. It is more permeable for I interstitials, allowing for diffusion of I into the CsPbBr_3 layer, as documented by a substantial occupancy of $\text{Pb}-\text{IBr}-\text{Pb}$ bridges there. The general conclusion then is that Br-rich interfaces hinder inter diffusion of halide species, whereas I-rich interfaces do not.

To further demonstrate the influence of defects on halide phase mixing in $\text{CsPb}(\text{I}_{x}\text{Br}_{1-x})_3$, we build models consisting of a $4 \times 4 \times 4$ cubic nanodomain of CsPbBr_3 inside a CsPbI_3 matrix (Figure 5a,b), and vice versa (Figure 5c,d). These model structures have six I-rich interfaces for I cubic nanodomains, and six Br-rich interfaces for Br cubic nanodomains. Starting with one halide point defect in the nanodomain, we perform 10 ns long MD runs at $T = 600$ K. The details of these MD runs are given in SI note 10. The final frames from the MD runs are analyzed for the number of halide atoms of the cubic nanodomain halide intermixed with one in the rest of the lattice.

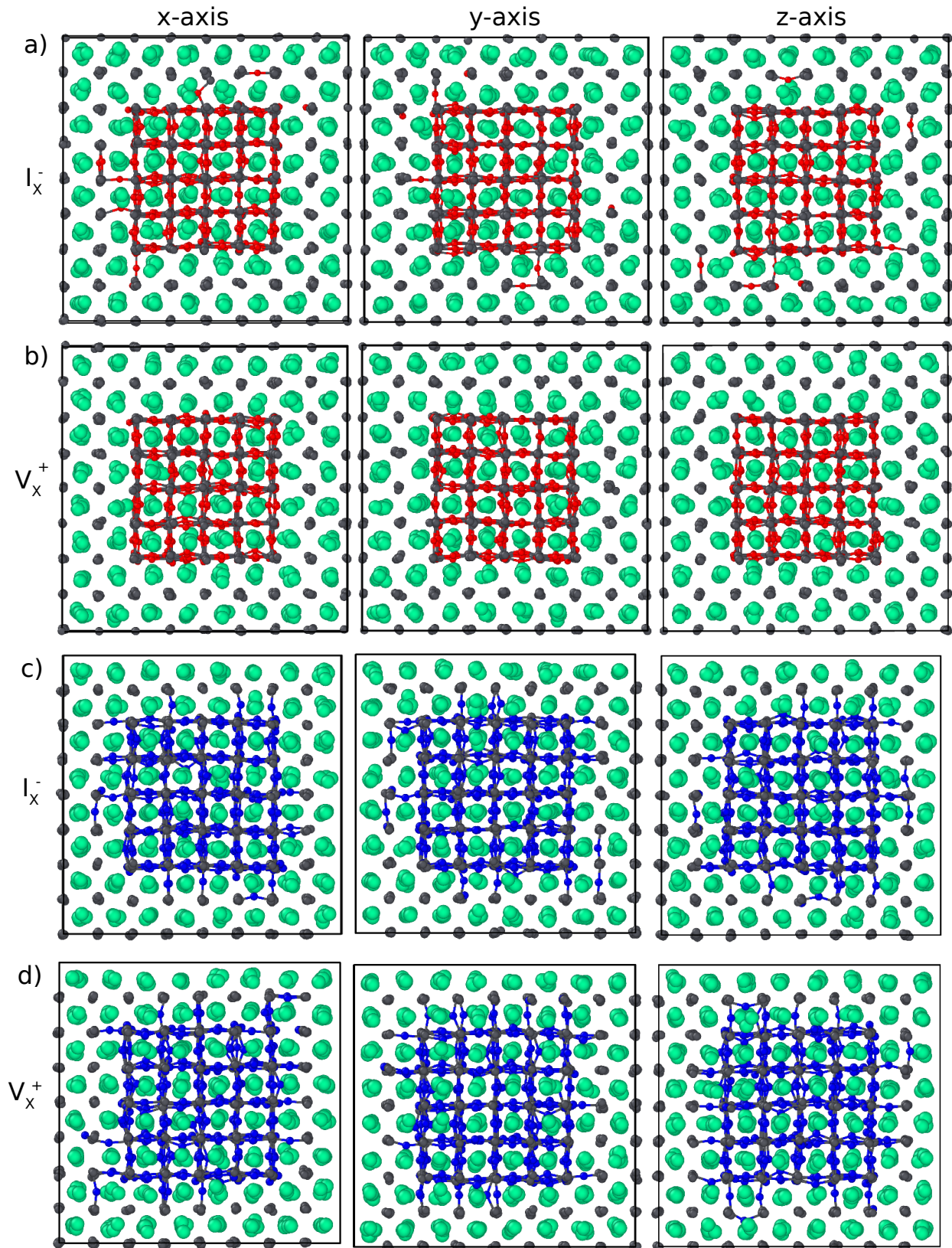


Figure 5: Final frames from the MD simulations along all three axes for (a) halide interstitial and (b) vacancy in Br cubic domain, and (c) halide interstitial and (d) vacancy in I cubic domain. The non-domain halide species atoms are omitted for the sake of clarity.

Starting with a vacancy in the CsPbBr_3 nanodomain (Figure 5b), no mixing events are observed in the 10 ns time frame. This is consistent with the interface studies discussed above, where the vacancy prefers to reside in the CsPbBr_3 phase, and Br-rich interfaces hinder the diffusion. Starting with an interstitial in a CsPbBr_3 nanodomain (Figure 5a), 11 mixing events are observed, which is compatible with the fact that Br-rich interfaces are more permeable for interstitials than for vacancies.

In contrast, the CsPbI_3 nanodomain is much more fragile, with 36 mixing events for the halide vacancy in the 10 ns time frame (Figure 5d), which is in line with the vacancy preferring the CsPbBr_3 phase, and I-rich interfaces being very permeable. For the halide interstitial 29 mixing events are observed (Figure 5b), stressing that the fragility of the CsPbI_3 nanodomain does not depend too much on whether diffusion is executed by halide vacancies or interstitials.

Summary and Conclusions

In summary, we study the diffusion of halide vacancies and interstitials in $\text{CsPb}(\text{I}_x\text{Br}_{1-x})_3$ and $\text{CsPbI}_3/\text{CsPbBr}_3$ heterojunctions. We trained a neural network potential for negatively charged halide interstitial and positively charged halide vacancy defects in $\text{CsPb}(\text{I}_x\text{Br}_{1-x})_3$ using DFT calculations. Using this force field, we performed ns-long MD simulations to study the migration behavior of these defects and their influence on halide mixing through interfaces and domains.

We observe enhanced diffusion of both vacancies and interstitials by a factor 2-3 at room temperature in the mixed halide compounds as compared to the single halide ones, where vacancies diffuse faster than interstitials by a factor of two. Our findings furthermore suggest that the preferred migrating halide species in $\text{CsPb}(\text{I}_x\text{Br}_{1-x})_3$ is different for interstitial and vacancy. At room temperature, bromide migrates an order of magnitude faster than iodide for interstitials, while iodide migrates a factor of five faster than bromide for vacancies.

These results are in qualitative agreement with experimental results on mixed $\text{MAPb}(\text{I}_x\text{Br}_{1-x})_3$, which displays enhanced halide migration compared to MAPbI_3 and MAPbBr_3 .⁵⁰ In addition, in the mixed-halide perovskite two diffusion coefficients are found, which we suggest could describe the migration of the Br and I ions respectively.

Diffusion across heterojunctions is governed by the interface structure, where a Br-rich interface blocks migration of vacancies in particular, and to a lesser extent for interstitials. An I-rich interface is much more permeable, both for interstitials, as well as for vacancies, and therefore facilitates diffusion and intermixing of halides. The latter is demonstrated by MD simulations on CsPbI_3 nanodomains in a CsPbBr_3 matrix and vice versa.

Acknowledgement

The authors thank Guus Bertens for his help with the compilation of LAMMPS with the `pair_allegro` patch. V.T. and S.T. acknowledge funding from Vidi (project no. VI.Vid.213.091) from the Dutch Research Council (NWO).

Supporting Information Available

Supporting information will be made available on publication.

Conflict of Interest

The authors declare no conflict of interest.

References

- (1) Liang, X.; Duan, D.; Al-Handawi, M. B.; Wang, F.; Zhou, X.; Ge, C.-y.; Lin, H.; Zhu, Q.; Li, L.; Naumov, P. et al. The Role of Ionic Liquids in Performance Enhancement of Two-Step Perovskite Photovoltaics. *Sol. RRL* **2023**, *7*, 2200856.

(2) Lin, K.; Xing, J.; Quan, L. N.; de Arquer, F. P. G.; Gong, X.; Lu, J.; Xie, L.; Zhao, W.; Zhang, D.; Yan, C. et al. Perovskite light-emitting diodes with external quantum efficiency exceeding 20 per cent. *Nature* **2018**, *562*, 245–248.

(3) Liu, Y.; Zhang, Y.; Yang, Z.; Feng, J.; Xu, Z.; Li, Q.; Hu, M.; Ye, H.; Zhang, X.; Liu, M. et al. Low-temperature-gradient crystallization for multi-inch high-quality perovskite single crystals for record performance photodetectors. *Mater. Today* **2019**, *22*, 67–75.

(4) Yi, C.; Luo, J.; Meloni, S.; Boziki, A.; Ashari-Astani, N.; Grätzel, C.; Zakeeruddin, S. M.; Röthlisberger, U.; Grätzel, M. Entropic stabilization of mixed A-cation ABX₃ metal halide perovskites for high performance perovskite solar cells. *Energy Environ. Sci.* **2016**, *9*, 656–662.

(5) Saliba, M.; Matsui, T.; Seo, J.-Y.; Domanski, K.; Correa-Baena, J.-P.; Nazeeruddin, M. K.; Zakeeruddin, S. M.; Tress, W.; Abate, A.; Hagfeldt, A. et al. Cesium-containing triple cation perovskite solar cells: improved stability, reproducibility and high efficiency. *Energy Environ. Sci.* **2016**, *9*, 1989–1997.

(6) Jung, Y.-K.; Lee, J.-H.; Walsh, A.; Soon, A. Influence of Rb/Cs Cation-Exchange on Inorganic Sn Halide Perovskites: From Chemical Structure to Physical Properties. *Chem. Mater.* **2017**, *29*, 3181–3188, PMID: 28435185.

(7) Näsström, H.; Becker, P.; Márquez, J. A.; Shargaieva, O.; Mainz, R.; Unger, E.; Unold, T. Dependence of phase transitions on halide ratio in inorganic CsPb(Br_xI_{1-x})₃ perovskite thin films obtained from high-throughput experimentation. *J. Mater. Chem. A* **2020**, *8*, 22626–22631.

(8) Liang, Z.; Xu, H.; Zhang, Y.; Liu, G.; Chu, S.; Tao, Y.; Xu, X.; Xu, S.; Zhang, L.; Chen, X. et al. A Selective Targeting Anchor Strategy Affords Efficient and Stable Ideal-Bandgap Perovskite Solar Cells. *Adv. Mater.* **2022**, *34*, 2110241.

(9) Kessels, L. M.; Remmerswaal, W. H. M.; Schipper, N. R. M.; Bellini, L.; Kwan, H.; Wienk, M. M.; Janssen, R. A. J. Tailoring the Crystallization Behavior of Mixed Lead-Tin Mixed-Halide Perovskites for Optimal-Bandgap Solar Cells. *Adv. Sci.* **2025**, *n/a*, e20948.

(10) Hoke, E. T.; Slotcavage, D. J.; Dohner, E. R.; Bowring, A. R.; Karunadasa, H. I.; McGehee, M. D. Reversible photo-induced trap formation in mixed-halide hybrid perovskites for photovoltaics. *Chem. Sci.* **2015**, *6*, 613–617, Publisher: The Royal Society of Chemistry.

(11) Wang, X.; Ling, Y.; Lian, X.; Xin, Y.; Dhungana, K. B.; Perez-Orive, F.; Knox, J.; Chen, Z.; Zhou, Y.; Beery, D. et al. Suppressed phase separation of mixed-halide perovskites confined in endotaxial matrices. *Nat. Commun.* **2019**, *10*, 695.

(12) Draguta, S.; Sharia, O.; Yoon, S. J.; Brennan, M. C.; Morozov, Y. V.; Manser, J. S.; Kamat, P. V.; Schneider, W. F.; Kuno, M. Rationalizing the light-induced phase separation of mixed halide organic–inorganic perovskites. *Nat. Commun.* **2017**, *8*, 200.

(13) Tang, X.; van den Berg, M.; Gu, E.; Horneber, A.; Matt, G. J.; Osset, A.; Meixner, A. J.; Zhang, D.; Brabec, C. J. Local Observation of Phase Segregation in Mixed-Halide Perovskite. *Nano Lett.* **2018**, *18*, 2172–2178, Publisher: American Chemical Society.

(14) Chen, Z.; Brocks, G.; Tao, S.; Bobbert, P. A. Unified theory for light-induced halide segregation in mixed halide perovskites. *Nat. Commun.* **2021**, *12*, 2687.

(15) Chen, Z.; Brocks, G.; Tao, S.; Bobbert, P. A. Light-tunable three-phase coexistence in mixed halide perovskites. *Phys. Rev. B* **2022**, *106*, 134110.

(16) Barker, A. J.; Sadhanala, A.; Deschler, F.; Gandini, M.; Senanayak, S. P.; Pearce, P. M.; Mosconi, E.; Pearson, A. J.; Wu, Y.; Srimath Kandada, A. R. et al. Defect-Assisted

Photoinduced Halide Segregation in Mixed-Halide Perovskite Thin Films. *ACS Energy Lett.* **2017**, *2*, 1416–1424, Publisher: American Chemical Society.

- (17) Xue, H.; Brocks, G.; Tao, S. First-principles calculations of defects in metal halide perovskites: A performance comparison of density functionals. *Phys. Rev. Mater.* **2021**, *5*, 125408.
- (18) Xue, H.; Brocks, G.; Tao, S. Intrinsic defects in primary halide perovskites: A first-principles study of the thermodynamic trends. *Phys. Rev. Mater.* **2022**, *6*, 055402.
- (19) Wang, F.; Bai, S.; Tress, W.; Hagfeldt, A.; Gao, F. Defects engineering for high-performance perovskite solar cells. *npj flex. electron.* **2018**, *2*, 22.
- (20) Ball, J. M.; Petrozzi, A. Defects in perovskite-halides and their effects in solar cells. *Nat. Energy* **2016**, *1*, 16149.
- (21) Eames, C.; Frost, J. M.; Barnes, P. R. F.; O'Regan, B. C.; Walsh, A.; Islam, M. S. Ionic transport in hybrid lead iodide perovskite solar cells. *Nat. Commun.* **2015**, *6*, 7497, Publisher: Nature Publishing Group.
- (22) Yu, H.; Lu, H.; Xie, F.; Zhou, S.; Zhao, N. Native Defect-Induced Hysteresis Behavior in Organolead Iodide Perovskite Solar Cells. *Adv. Funct. Mater.* **2016**, *26*, 1411–1419, eprint: <https://advanced.onlinelibrary.wiley.com/doi/pdf/10.1002/adfm.201504997>.
- (23) Li, C.; Tscheuschner, S.; Paulus, F.; Hopkinson, P. E.; Kießling, J.; Köhler, A.; Vaynzof, Y.; Huettner, S. Iodine Migration and its Effect on Hysteresis in Perovskite Solar Cells. *Adv. Mater.* **2016**, *28*, 2446–2454, eprint: <https://advanced.onlinelibrary.wiley.com/doi/pdf/10.1002/adma.201503832>.
- (24) Game, O. S.; Buchsbaum, G. J.; Zhou, Y.; Padture, N. P.; Kingon, A. I. Ions Matter: Description of the Anomalous Electronic Behavior in Methylammonium

Lead Halide Perovskite Devices. *Adv. Funct. Mater.* **2017**, *27*, 1606584, eprint: <https://advanced.onlinelibrary.wiley.com/doi/pdf/10.1002/adfm.201606584>.

(25) Schmidt, M. C.; Alvarez, A. O.; Pallotta, R.; Seid, B. A.; de Boer, J. J.; Thiesbrummel, J.; Lang, F.; Grancini, G.; Ehrler, B. Quantification of Mobile Ions in Perovskite Solar Cells with Thermally Activated Ion Current Measurements. *ACS Energy Lett.* **2026**, *11*, 409–418.

(26) Mosconi, E.; Meggiolaro, D.; Snaith, H. J.; Stranks, S. D.; De Angelis, F. Light-induced annihilation of Frenkel defects in organo-lead halide perovskites. *Energy Environ. Sci.* **2016**, *9*, 3180–3187.

(27) Sarkar, G.; Ghosh, D. Effects of Lattice Compression on Halogen Ion Diffusion Dynamics in Mixed Halide Perovskites. *ACS Appl. Energy Mater.* **2024**, *7*, 6376–6383.

(28) Sarkar, G.; Deswal, P.; Ghosh, D. Ion Diffusion Dynamics and Halogen Mixing at the Heterojunction of Halide Perovskites: Atomistic Insights. *J. Phys. Chem. C* **2024**, *128*, 1762–1772.

(29) Behler, J. Four Generations of High-Dimensional Neural Network Potentials. *Chem. Rev.* **2021**, *121*, 10037–10072, PMID: 33779150.

(30) Unke, O. T.; Chmiela, S.; Sauceda, H. E.; Gastegger, M.; Poltavsky, I.; Schütt, K. T.; Tkatchenko, A.; Müller, K.-R. Machine Learning Force Fields. *Chem. Rev.* **2021**, *121*, 10142–10186, PMID: 33705118.

(31) Wu, S.; Yang, X.; Zhao, X.; Li, Z.; Lu, M.; Xie, X.; Yan, J. Applications and Advances in Machine Learning Force Fields. *J. Chem. Inf. Model.* **2023**, *63*, 6972–6985, PMID: 37751546.

(32) Mosquera-Lois, I.; Klarbring, J.; Walsh, A. Point defect formation at finite temperatures with machine learning force fields. *Chem. Sci.* **2025**, *16*, 8878–8888.

(33) Bartók, A. P.; Kondor, R.; Csányi, G. On representing chemical environments. *Phys. Rev. B* **2013**, *87*, 184115.

(34) Jinnouchi, R.; Lahnsteiner, J.; Karsai, F.; Kresse, G.; Bokdam, M. Phase Transitions of Hybrid Perovskites Simulated by Machine-Learning Force Fields Trained on the Fly with Bayesian Inference. *Phys. Rev. Lett.* **2019**, *122*, 225701.

(35) Jinnouchi, R.; Karsai, F.; Kresse, G. On-the-fly machine learning force field generation: Application to melting points. *Phys. Rev. B* **2019**, *100*, 014105.

(36) Jinnouchi, R.; Karsai, F.; Verdi, C.; Asahi, R.; Kresse, G. Descriptors representing two- and three-body atomic distributions and their effects on the accuracy of machine-learned inter-atomic potentials. *J. Chem. Phys.* **2020**, *152*, 234102.

(37) Tyagi, V.; Pols, M.; Brocks, G.; Tao, S. Tracing Ion Migration in Halide Perovskites with Machine Learned Force Fields. *J. Phys. Chem. Lett.* **2025**, *16*, 5153–5159.

(38) Schütt, K.; Kindermans, P.-J.; Sauceda Felix, H. E.; Chmiela, S.; Tkatchenko, A.; Müller, K.-R. SchNet: A continuous-filter convolutional neural network for modeling quantum interactions. Advances in Neural Information Processing Systems. 2017.

(39) Batzner, S.; Musaelian, A.; Sun, L.; Geiger, M.; Mailoa, J. P.; Kornbluth, M.; Molinari, N.; Smidt, T. E.; Kozinsky, B. E(3)-equivariant graph neural networks for data-efficient and accurate interatomic potentials. *Nat. Comm.* **2022**, *13*, 2453.

(40) Musaelian, A.; Batzner, S.; Johansson, A.; Sun, L.; Owen, C. J.; Kornbluth, M.; Kozinsky, B. Learning local equivariant representations for large-scale atomistic dynamics. *Nat. Comm.* **2023**, *14*, 579.

(41) Geiger, M.; Smidt, T. e3nn: Euclidean neural networks. *arXiv preprint arXiv:2207.09453* **2022**,

(42) Kresse, G.; Furthmüller, J. Efficient iterative schemes for ab initio total-energy calculations using a plane-wave basis set. *Phys. Rev. B* **1996**, *54*, 11169–11186.

(43) Perdew, J. P.; Burke, K.; Ernzerhof, M. Generalized Gradient Approximation Made Simple. *Phys. Rev. Lett.* **1996**, *77*, 3865–3868.

(44) Grimme, S.; Ehrlich, S.; Goerigk, L. Effect of the damping function in dispersion corrected density functional theory. *J. Comput. Chem.* **2011**, *32*, 1456–1465.

(45) Henkelman, G.; Uberuaga, B. P.; Jónsson, H. A climbing image nudged elastic band method for finding saddle points and minimum energy paths. *The Journal of Chemical Physics* **2000**, *113*, 9901–9904.

(46) Thompson, A. P.; Aktulga, H. M.; Berger, R.; Bolintineanu, D. S.; Brown, W. M.; Crozier, P. S.; in 't Veld, P. J.; Kohlmeyer, A.; Moore, S. G.; Nguyen, T. D. et al. LAMMPS - a flexible simulation tool for particle-based materials modeling at the atomic, meso, and continuum scales. *Comp. Phys. Comm.* **2022**, *271*, 108171.

(47) Meggiolaro, D.; De Angelis, F. First-Principles Modeling of Defects in Lead Halide Perovskites: Best Practices and Open Issues. *ACS Energy Lett.* **2018**, *3*, 2206–2222.

(48) Ganster, P.; Tréglia, G.; Saúl, A. Strain effect on self-diffusion in silicon: Numerical study. *Phys. Rev. B* **2009**, *79*, 115205.

(49) Kawamura, Y.; Uematsu, M.; Hoshi, Y.; Sawano, K.; Myronov, M.; Shiraki, Y.; Haller, E. E.; Itoh, K. M. Self-diffusion in compressively strained Ge. *Journal of Applied Physics* **2011**, *110*, 034906.

(50) McGovern, L.; Grimaldi, G.; Futscher, M. H.; Hutter, E. M.; Muscarella, L. A.; Schmidt, M. C.; Ehrler, B. Reduced Barrier for Ion Migration in Mixed-Halide Perovskites. *ACS Applied Energy Materials* **2021**, *4*, 13431–13437.